

Tuning the magnetocaloric and structural properties of $La_{0.67}Sr_{0.28}Pr_{0.05}Mn_{1-x}Co_xO_3$ refrigeration materials

Changji Xu(徐长吉), Xinyu Jiang(姜心雨), Zhengguang Zou(邹正光), Zhuojia Xie(谢卓家), Weijian Zhang(张伟建), and Min Feng(冯敏)

Citation: Chin. Phys. B, 2024, 33 (**12**): 127501. DOI: 10.1088/1674-1056/ad8550
Journal homepage: http://cpb.iphy.ac.cn; http://iopscience.iop.org/cpb

What follows is a list of articles you may be interested in

Magnetocaloric properties of Nd-doped Gd_5Si_4 microparticles and nanopowders

Kaiyang Zhang(张凯扬), Huanhuan Wang(王欢欢), Ying Wang(王颖), and Tao Wang(王涛)
Chin. Phys. B, 2024, 33 (**11**): 117502. DOI: 10.1088/1674-1056/ad6de7

Magnetic and magnetocaloric effect of $Er_{20}Ho_{20}Dy_{20}Cu_{20}Ni_{20}$ high-entropy metallic glass

Shi-Lin Yu(于世霖), Lu Tian(田路), Jun-Feng Wang(王俊峰), Xin-Guo Zhao(赵新国), Da Li(李达), Zhao-Jun Mo(莫兆军), and Bing Li(李昺)
Chin. Phys. B, 2024, 33 (**5**): 057502. DOI: 10.1088/1674-1056/ad1a94

Structure, magnetism and magnetocaloric effects in $Er_5Si_3B_x$ (x=0.3, 0.6) compounds

Zhihong Hao(郝志红), Hui Liu(刘辉), and Juguo Zhang(张聚国)
Chin. Phys. B, 2023, 32 (**11**): 117501. DOI: 10.1088/1674-1056/ace684

Giant low-field cryogenic magnetocaloric effect in polycrystalline $LiErF_4$ compound

Zhaojun Mo(莫兆军), Jianjian Gong(巩建建), Huicai Xie(谢慧财), Lei Zhang(张磊), Qi Fu(付琪), Xinqiang Gao(高新强), Zhenxing Li(李振兴), and Jun Shen(沈俊)
Chin. Phys. B, 2023, 32 (**2**): 027503. DOI: 10.1088/1674-1056/ac65ef

Magnetocaloric properties of phenolic resin bonded $La(Fe,Si)_{13}$-based plates and its use in a hybrid magnetic refrigerator

Shao-Shan Xu(徐少山), Qi Fu(付琪), Yi-Fan Zhou(周益帆), Ling Peng(彭铃), Xin-Qiang Gao(高新强), Zhen-Xing Li(李振兴), Mao-Qiong Gong(公茂琼), Xue-Qiang Dong(董学强), and Jun Shen(沈俊)
Chin. Phys. B, 2023, 32 (**2**): 027502. DOI: 10.1088/1674-1056/ac9fbf

---

Tuning the magnetocaloric and structural properties of $La_{0.67}Sr_{0.28}Pr_{0.05}Mn_{1-x}Co_xO_3$ refrigeration materials

Changji Xu(徐长吉)[1], Xinyu Jiang(姜心雨)[1], Zhengguang Zou(邹正光)[1,2,†], Zhuojia Xie(谢卓家)[1], Weijian Zhang(张伟建)[1], and Min Feng(冯敏)[1]

[1] *College of Materials Science and Engineering, Guilin University of Technology, Guilin* 541004, *China*
[2] *Collaborative Innovation Center for Exploration of Hidden Nonferrous Metal Deposits and Development of New Materials, Guilin University of Technology, Guilin* 541004, *China*

(Received 21 June 2024; revised manuscript received 10 September 2024; accepted manuscript online 10 October 2024)

The structural, magnetic and magnetocaloric properties of perovskite manganites $La_{0.67}Sr_{0.28}Pr_{0.05}Mn_{1-x}Co_xO_3$ ($x =$ 0.05, 0.075 and 0.10) (LSPMCO) are investigated. LSPMCO crystallizes as a rhombohedral structure with *R*-3*c* space group. As the Co content increases, the cell volume expands, the Mn–O–Mn bond angle reduces and the length of the Mn–O bond increases. The samples show irregular submicron particles under a Zeiss scanning electron microscopy. The particle size becomes larger with increasing doping. The chemical composition of the samples is confirmed by x-ray photoelectron spectroscopy (XPS). The ferromagnetic (FM) to paramagnetic (PM) phase transition occurs near the Curie temperature (T_C), and all transitions are second-order phase transitions (SMOPT) characterized by minimal thermal and magnetic hystereses. Critical behavior analysis indicates that the critical parameters of LSPMCO closely align with those predicted by the mean-field model. The T_C declines with Co doping and reaches near room temperature (302 K) at $x = 0.075$. The maximum magnetic entropy change ($-\Delta S_M^{max}$) at $x = 0.05$ is 4.27 J/kg·K, and the relative cooling power (RCP) peaks at 310.81 J/K. Therefore, the system holds significant potential for development as a magnetic refrigeration material, meriting further professional and objective evaluation.

Keywords: magnetic refrigeration, perovskite manganites, second-order phase transitions, relative cooling power, magnetocaloric effect

PACS: 75.30.Sg, 75.30.–m, 75.47.Lx, 75.10.–b **DOI:** 10.1088/1674-1056/ad8550

1. Introduction

Magnetic refrigeration, employing the magnetocaloric effect, presents significant prospects for tackling urgent concerns related to climate change, energy efficiency and heat management.[1–4] Magnetic cooling based on the magnetocaloric effect (MCE) has attracted great interest as a technique to reduce global warming. Magnetic refrigeration finds application in various aspects of human life, including but not limited to daily necessities, healthcare and industrial production. Improving cooling performance is important, with about half of all data servers requiring cooling to keep them running while they are in operation.[5–8]

Compared with traditional gas compression refrigeration technology, magnetic refrigeration technology has several advantages such as higher efficiency and green energy saving. In addition, no ozone-depleting chemicals are used and there is a reduction in noise and vibration.[9,10] Because of its unique physical characteristics, the magnetostatic effect holds potential as an environmentally friendly technology for refrigeration.[11] Hundreds of MCE materials have been identified, and dozens of potential MCE materials are still being researched and described annually. $La(FeSi)_{13}$ alloys, Gd-based alloys and Mn-based alloys, among others, have shown excellent MCE values.[12] Nevertheless, there are some disadvantages to these materials. For example, Gd-based alloys tend to be relatively expensive, some Mn-based alloys involve toxic raw materials, $La(FeSi)_{13}$ alloys exhibit magnetic and thermal hysteresis, and the synthesis methods for these materials can be cumbersome. Perovskite manganites have been the subject of intensive research for many years as materials to promote refrigeration due to the large change in magnetic entropy, small thermomagnetic hysteresis and relatively low cost.[13,14]

The tuning of the properties of perovskite manganites relies heavily on doping. The perovskite manganites can be represented by the chemical formula ABO_3, where *A* represents a rare-earth lanthanide element and *B* is a trivalent manganese ion.[15–17] The categorization of property tuning includes *A*-site, *B*-site and *AB*-site doping. The main adjustment of the energy by *A*-site doping is attributed to the distortion of the lattice due to the difference in ionic radii. The distortion of the lattice affects the bandwidth and thus the double exchange (DE) interaction further to the magnetic entropy change (ΔS_M). Previous research work involved the preparation and characterization of perovskite manganites $LnMnO_3$, where *Ln* is a rare-earth ion such as La, Pr and Nd, an alkaline earth ion such as Sr, Ca and Ba, or a combination of these ions. The doped perovskite manganites have relatively desirable properties.[18,19] *B*-site doping differs from *A*-site doping

†Corresponding author. E-mail: zouzgglut@163.com

© 2024 Chinese Physical Society and IOP Publishing Ltd

in that the *B*-site directly affects the Mn^{3+}/Mn^{4+} ratio. Doping transition metals, including Fe, Co, Cu and Cr, at the *B* site, induce notable structural, magnetic and resistive alterations via network modification.

2. Experimental details

The sol–gel method was used in this paper as a relatively mature preparation process. The raw materials are $La(NO_3)_3{\cdot}6H_2O$, $Sr(NO_3)_2$, $Pr(NO_3)_3{\cdot}6H_2O$, $Mn(NO_3)_2$ (50%) and $Co(NO_3)_2{\cdot}6H_2O$ (all chemicals are the Aladdin brand with $\geq 99.5\%$ purity). An appropriate amount of citric acid and ethanediol was added as a complexing agent after the ingredients were completely dissolved. A wet gel was obtained by heating in a water bath and then drying at 393 K to obtain a dry gel. It was then pre-sintered at 574 K so that the organic matter was removed from the sample. It was cooled to room temperature and then ground. The samples were sintered in a muffle furnace at 1274 K to obtain the final samples.

The LSPMCO sample was characterized. The structure, phases and crystal parameters were analyzed using x-ray diffraction (XRD) with Cu $K\alpha_1$ radiation ($\lambda = 1.54059$ Å). Further processing of the LSPMCO data was carried out using detailed Rietveld analysis. A Thermo Nicolet NEXUS 670 spectrometer was used to examine the molecular structure and chemical composition of the samples.

The morphological characteristics of the samples were observed via scanning electron microscopy (SEM), while the compositional allocation of the samples was analyzed by employing energy dispersive spectroscopy (EDS). The magnetic properties were evaluated using the integrated magnetic measurement system.

3. Results and analysis

3.1. Structural analysis

The crystal structure parameters of the sample were investigated by x-ray diffraction analysis. XRD data of LSPMCO at room temperature are presented in Fig. 1. Figure 1 confirms that all doping gradients of LSPMCO are single-phase structures. The position and intensity of the diffraction peaks can be analyzed for the presence of other impurity phases and the degree of crystallization of the sample. Refinement of the XRD data of LSPMCO by GSAS confirms that LSPMCO has the rhombic structure with the *R*-3*c* space group (No. 167).

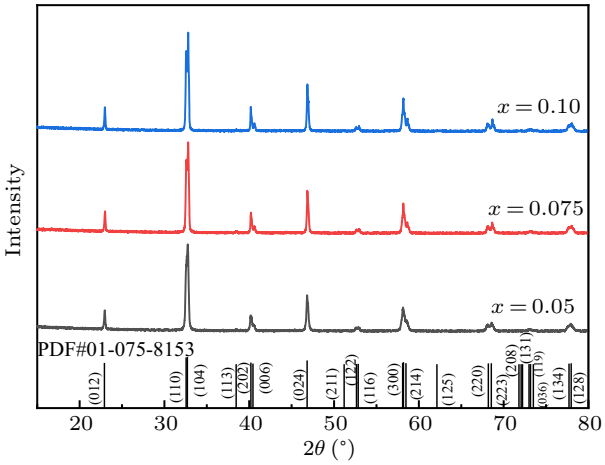


Fig. 1. X-ray powder diffraction pattern of LSPMCO.

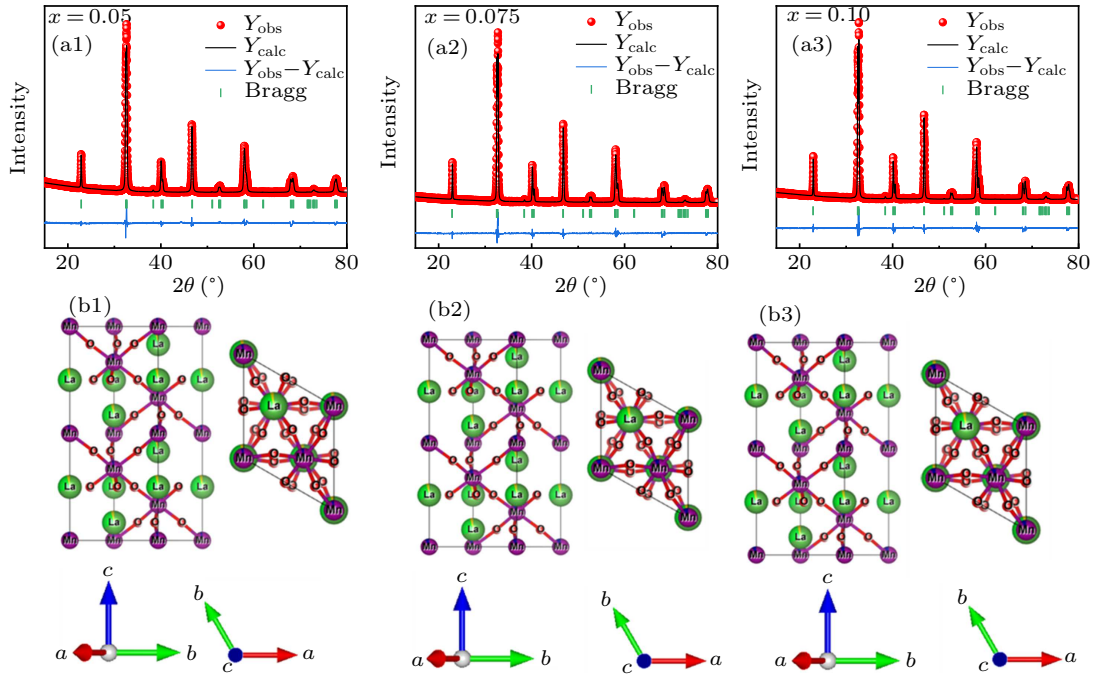


Fig. 2. (a1)–(a3) Rietveld refinement of the XRD pattern. (b1)–(b3) Cell structure of the samples.

Table 1. Refined structural parameters of LSPMCO.

x	0.05	0.075	0.10
Space group	*R*-3*c*	*R*-3*c*	*R*-3*c*
$a = b$ (Å)	5.514731	5.515489	5.516912
c (Å)	13.371766	13.379537	13.392511
V (Å^3)	352.176	352.484	353.008
Mn–O (Å)	1.95446	1.95502	1.95598
Mn–O–Mn (°)	167.694	169.692	167.690
R_p (%)	2.24	2.26	2.45
R_{wp} (%)	3.24	3.15	3.27
χ^2	4.451	3.965	3.759
t	0.9620	0.9614	0.9607
W (10^{-2} a.u.)	13.086	13.075	13.056
D_{XRD} (nm)	43.47	53.53	66.91

The refined data plots and crystal structures for each doping level are presented in Fig. 2. Table 1 lists the lattice constants, cell volume (V), Mn–O bond lengths and Mn–O–Mn bond angles, which provide a summary of the goodness of fit χ^2. V enhances with increasing Co^{2+} dopant amount. The reason for this is that the ionic radius of Co^{2+} (0.745 Å) is larger than the ionic radius of Mn^{3+} (0.645 Å). Meanwhile, the length of the Mn–O bond increases, and the angle of the Mn–O–Mn bond reduces, leading to the deformation of the LSPMCO lattice. To further understand the level of distortion of the LSPMCO crystal structure after doping with Co^{2+}, the tolerance factor (t) proposed by Goldschmidt is used. The formula is as follows:

$$t = \frac{(r_A + r_O)}{\sqrt{2}(r_B + r_O)}, \tag{1}$$

where r_O, r_B and r_A are the oxygen-site ionic radius, B-site mean ionic radius and A-site mean ionic radius, respectively. When $0.89 < t < 1.02$, the perovskite structure can be stabilized; when $0.96 < t < 1.00$, the samples exist as rhombohedral structure. The Shannon formula was used to calculate the average ionic radius size.[20] The calculated t ranged from 0.96 to 1, confirming that LSPMCO is a rhombohedral structure.

3.2. Morphology analysis

Figure 3(a) shows the microscopic morphology of LSPMCO, which is presented as irregular polyhedral particles with some agglomerations, as can be seen from the figure. LSPMCO is micron-sized particles with an average particle size of 300 nm–180 nm. The average grain size (D_{XRD}) of LSPMCO was calculated by Scherrer's formula[21]

$$D_{XRD} = \frac{K\lambda}{\beta \cos(\theta)}. \tag{2}$$

Here, Scherrer's constant is denoted as K and its numerical value is 0.9. The length of the x-rays is denoted by λ, which has a value of 0.15406 nm. θ is the angle of Bragg diffraction and β refers to the half-height width of the diffraction peak observed in LSPMCO. The D_{XRD} of LSPMCO was 43.47 nm, 53.53 nm and 66.91 nm, respectively. The trend is the same for D_{XRD} and D_{SEM}, which both become larger with more doping. It was found that the grain size attained by SEM tests was larger than that of the D_{XRD} attained by the calculation of Scherrer's formula. The possible reason for this is that the particles observed in the SEM images may have multiple crystal domains, which are caused by defects or internal stresses within the particles.[22] Thus, the data obtained are larger than those of the D_{XRD}. Figure 3(b) shows the total elemental spectrum obtained from the EDS test, illustrating that LSPMCO contains all the expected elements (La, Pr, Sr, Mn, Co, O). Figure 4 demonstrates that not only do the samples contain all the expected elements, but each element is uniformly distributed.

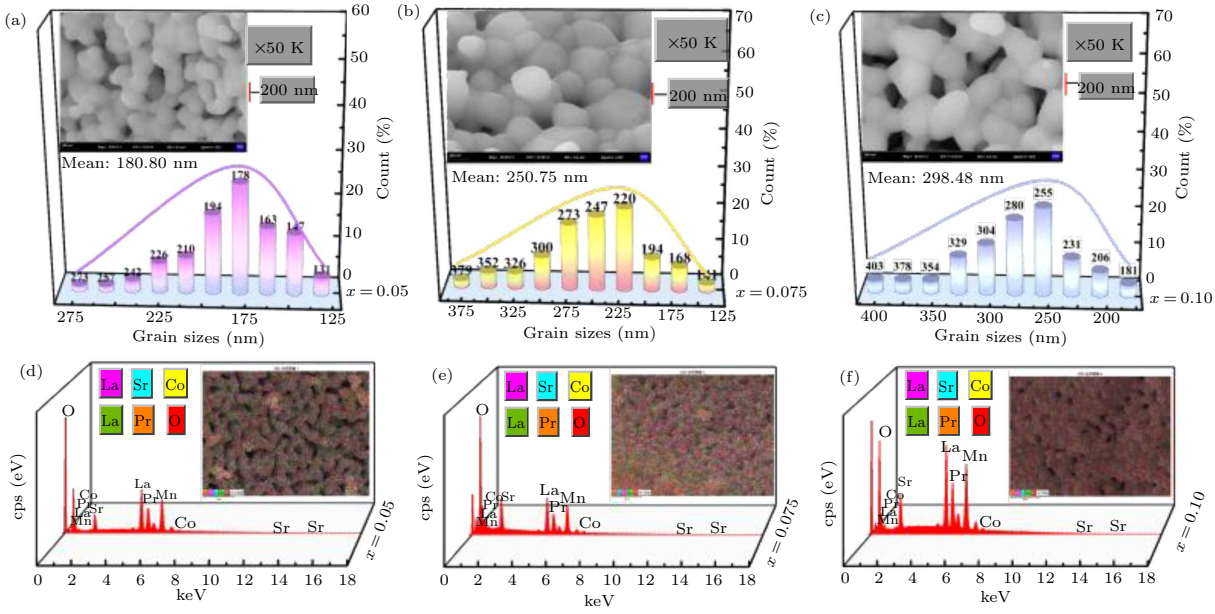


Fig. 3. Morphology and grain size distribution of LSPMCO (a) $x = 0.05$, (b) $x = 0.075$, (c) $x = 0.10$. Elemental distribution of LSPMCO (d) $x = 0.05$, (e) $x = 0.075$, (f) $x = 0.10$.

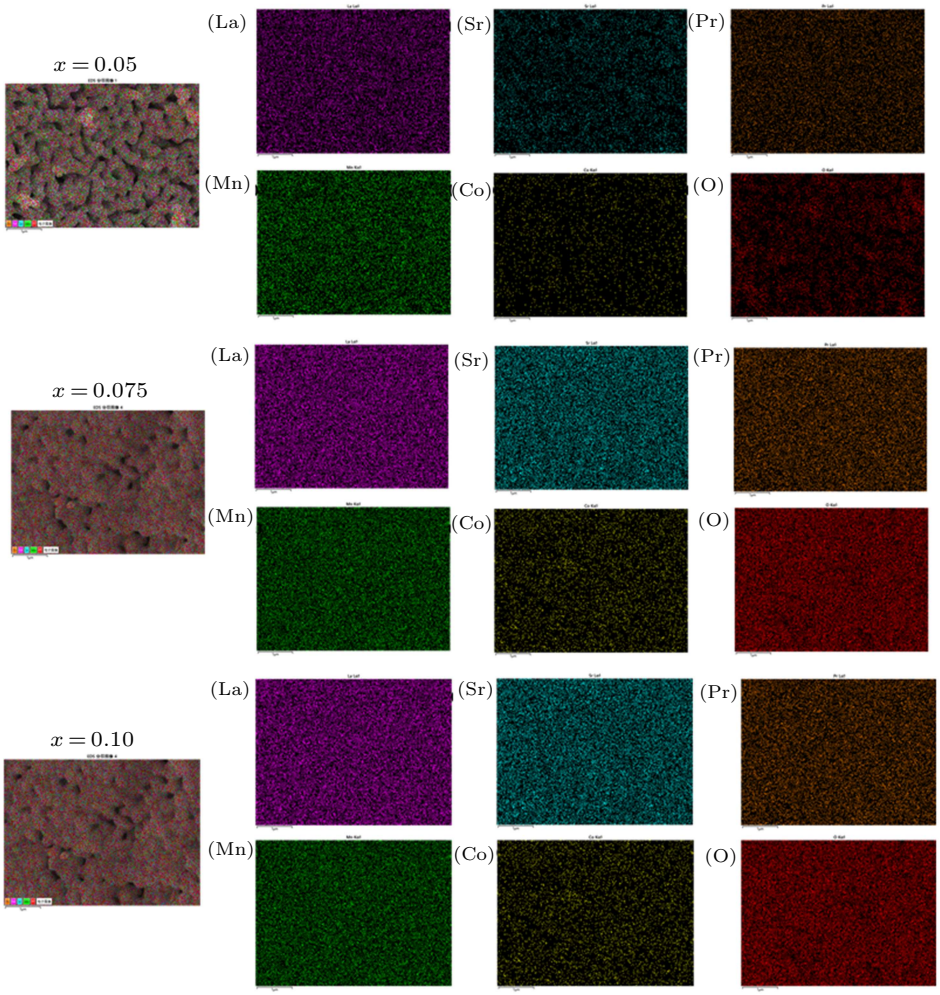


Fig. 4. Mapping of the distribution of elements.

3.3. FT-infrared spectroscopic analysis

Figure 5 shows the Fourier infrared spectral absorption diagram of the product, through which the crystal structure of the particles was investigated from the point of view of lattice vibrations. The MnO_6 ion is widely recognized to exhibit octahedral symmetry within the manganite structure. This symmetry is often reflected by prominent infrared (IR) bands that are active at 600 cm^{-1}.[23] The strong absorption peaks are due to the vibrations of the Mn–O bonds. The absorption bands at 600 cm^{-1} and 492 cm^{-1} represent the stretching (ν_s) and bending (ν_b) vibrational modes of the Mn–O bond, respectively. ν_s is relevant to the Mn–O bond length and ν_b is relevant to the size of the Mn–O–Mn bond angle.[24] With the increase in doping, its intensity decreases and the frequency remains constant. This shows that the vibrational volume content of the Mn–O bond decreases due to the deformation of the structure. There are also two weak absorption bands observed near 1380 cm^{-1} and 1635 cm^{-1}, and a broader absorption band appears near 3430 cm^{-1}. Two weak absorption bands were observed due to the asymmetric stretching vibration of the C=C bond (1380 cm^{-1}) and the symmetric stretching vibration of C=O (1635 cm^{-1}).[25,26] The C=C and C=O functional groups are derived from citric acid and ethylene glycol solvents added as complexing agents. A very broad peak was observed near 3454 cm^{-1}, leading to a stretching vibration of the hydroxyl group.[27,28] The broad absorption drop in the 3454 cm^{-1} band is associated with symmetric and asymmetric tensile vibration of the hydroxyl groups (O–H) of water molecules adsorbed on the surface. This is caused by exposure of the sample to vapor in the air.[29,30] IR spectra showed the presence of Mn–O

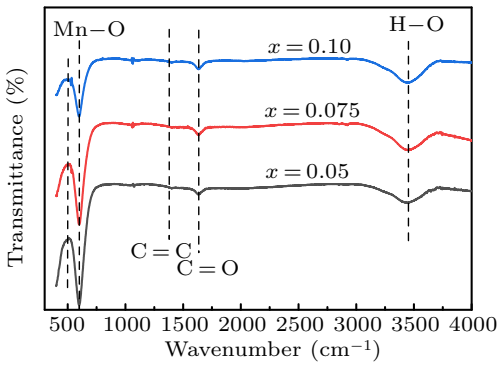


Fig. 5. FT-IR absorption spectra of $La_{0.67}Sr_{0.28}Pr_{0.05}Mn_{1-x}Co_xO_3$ ($x = 0.05$, 0.075 and 0.10).

bonds in the Co-doped nanoparticles, indicating the formation of a MnO_6 octahedral structure. This is consistent with the XRD results.

3.4. XPS analysis

XPS measurements are carried out to deeply comprehend the elemental distribution of the $La_{0.67}Sr_{0.28}Pr_{0.05}Mn_{1-x}Co_xO_3$ surface and its ionic valence states.

Figure 6 displays the contrast between the wide scans for all samples. In the diagram, we find that with the increase in Co doping, the core level is enhanced significantly. The core level of Mn shows the opposite trend. Figure 6 shows the deconvolution high-resolution spectra of La 3d, Sr 3d, Pr 3d, Mn 2p, Co 2p and O 1s for LSPMCO ($x = 0.05$, 0.075 and 0.10) samples.

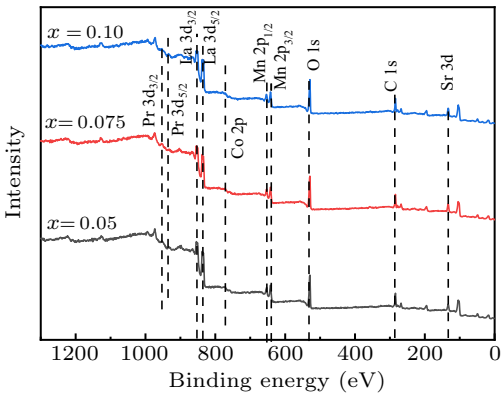


Fig. 6. The contrast between the wide scans for all samples.

Figure 7(a) presents a schematic of the fine spectrum of the La 3d core level in LSPMCO. The spectrum reveals two prominent doublets corresponding to La $3d_{3/2}$ and La $3d_{5/2}$. The two peaks near 836 eV correspond to La $3d_{5/2}$, and the two peaks at 853 eV correspond to the spin–orbit component of La $3d_{3/2}$. The first splitting arises from spin–orbit interactions, whereas the second splitting is attributed to electron transfer from the oxygen valence band to the unoccupied La 4f energy level. The presence of an additional peak could be attributed to vibrational excitations.[31]

In addition, Fig. 7(b) displays the peak diagram for the Sr element. The peak of 132.31 eV is Sr $3d_{5/2}$. The binding energy of this peak may tell us that $SrCO_3$ is present in the samples, which may be caused by sintering. The peak of 134.05 eV is Sr $3d_{3/2}$. The presence of this peak proves that $Sr(NO_3)_2$ may be present in the sample, and the cause of this phenomenon may be the presence of excess Sr ions.

Figure 7(c) is the XPS plot for Pr^{3+}. The XPS spectrum of Pr 3d shows two groups of spin–orbit multiples with binding energies of about 953.7 eV and 935.0 eV, representing the $3d_{3/2}$ and $3d_{5/2}$ electrons of Pr, respectively. The binding energies of Pr ($3d_{5/2}$) are about 935.3 for the 4-valent, around 933.3 for the 3-valent, and 934.5 eV for the 4-valent, which have also been reported in the literature.[32–34] Otherwise, more vibrational satellite peaks are generated due to the low content of Pr and Cu 2p interfering with it. The binding energy of the Pr^{3+} peak is larger than that of the Pr^{4+} peak, and the results indicate that the Pr^{3+} state dominates the structure.

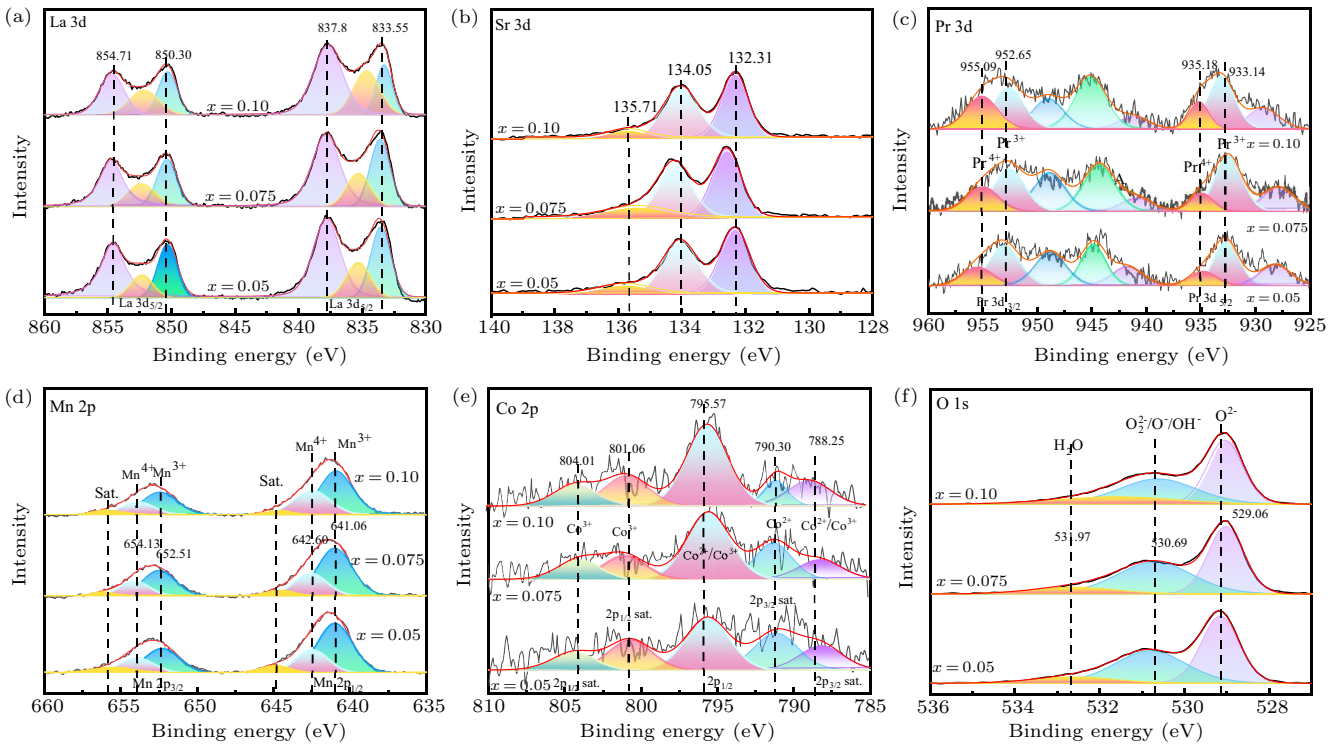


Fig. 7. The XPS spectra of $La_{0.67}Sr_{0.28}Pr_{0.05}Mn_{1-x}Co_xO_3$ ($x = 0.05$, 0.075 and 0.10).

In Fig. 7(d), resolving the spectrum according to the simplest symmetry model based on the splitting of the peaks of Mn is not precise enough.[35,36] From the figure, it can be seen that the samples include three components, Mn^{4+}, Mn^{3+} and a satellite peak, and Mn^{2+} is not observed on the surface of all the samples.[37] The asymmetry of the peaks indicates the existence of multiple components. The Mn $2p_{3/2}$ spectra are decomposed as two components. The first peak at 641.06 eV is associated with Mn^{3+}, while the second peak at 642.60 eV can be assigned to Mn^{4+}. The appearance of a satellite peak at 644.85 eV deeply verifies the presence of Mn^{4+}.[34,38] Mn $2p_{1/2}$ at 653.19 eV also supports the above statement, and similar results are obtained in the literature.[39] The positions of Mn^{3+} and Mn^{4+} and binding energies are shifted with increasing Co^{2+} doping, and the proportion of Mn^{4+} to Mn^{3+} is boosted, with the specific values listed in Table 2. The rise in the Mn^{4+}/Mn^{3+} ratio enhances the superexchange (SE) interactions within the samples, which competes with double exchange (DE), leading to a weakening of DE and thereby influencing the material's properties.

Figure 7(e) is an XPS plot of elemental Co. It is evident from the figure that the XPS peak of Co is significantly enhanced with the increase in Co doping. According to the previous explorations of Co, there are supposed to be two valence states, Co^{2+} and Co^{3+}, which are also verified from the peaks and vibrational peaks in Fig. 7(e).[40–42] The dissimilar valence states of $Co^{2+}$and Mn^{3+} directly change the carrier density of the system, and the performance can be modulated.

Figure 7(f) is an XPS plot of O 1s, which has three peaks in total. The peak near 529.06 eV is probably due to the simultaneous existence of oxygen in the manganese lattice in the sample, the peak at 530.60 eV could be oxygen adsorbed on the surface of the sample and hydroxyl groups on the surface or weakly bound oxygen on the surface, and the peak at 531.97 eV may indicate the presence of some H_2O.[43,44]

Table 2. The fitting parameters of the Mn 2p peaks for LSPMCO.

x	Mn $2p_{1/2}$ Mn^{3+}	Mn $2p_{1/2}$ Mn^{4+}	Mn $2p_{3/2}$ Mn^{3+}	Mn $2p_{3/2}$ Mn^{4+}	Mn^{4+}/Mn^{3+}
0.05	652.31	653.92	641.00	642.51	0.3087
0.075	652.50	654.10	641.06	642.60	0.3269
0.10	652.45	653.95	640.94	642.53	0.3424

3.5. Magnetic property analysis

This study investigates the magnetic phase transitions of LSPMCO samples, focusing on the effects of Co^{2+} substitution on the behavior of the M–T curve. The DC magnetization is measured as a function of temperature and the M–T curves are performed at temperatures from 230–350 K with an applied magnetic field, as shown in Fig. 8, where it can be seen that the M-value of the LSPMCO samples decreases sharply with the increase in T in a certain temperature interval. This confirms the occurrence of FM–PM phase transition in the samples.

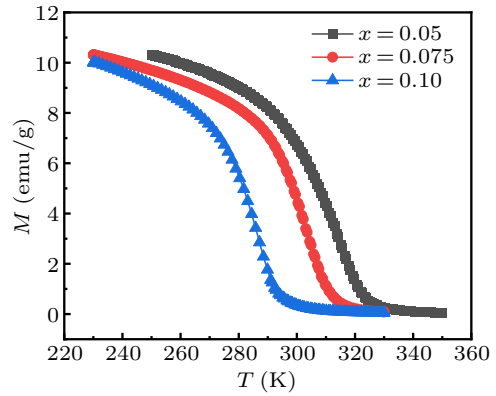


Fig. 8. Temperature dependence of magnetization for $La_{0.67}Sr_{0.28}Pr_{0.05}Mn_{1-x}Co_xO_3$ measured as $H = 100$ Oe.

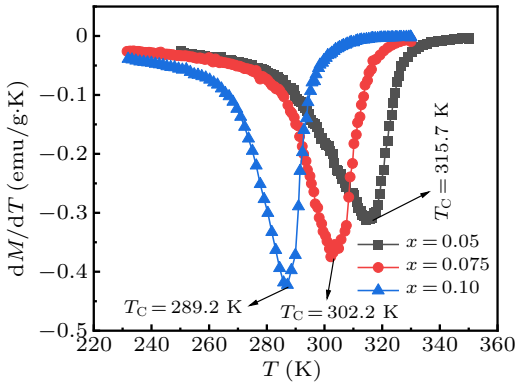


Fig. 9. The dM/dT–T curves of $La_{0.67}Sr_{0.28}Pr_{0.05}Mn_{1-x}Co_xO_3$ (x = 0.05, 0.075 and 0.10).

Using the derivative of the M–T curve, the extreme point of the dM/dT versus T curve (as shown in Fig. 9) corresponds to the T_C. As the Co^{2+} content (x) increases, the T_C values are observed to be 315.7 K, 302.2 K and 297.2 K, respectively.

The change in T_C is influenced by two factors: structural distortion and fluctuations in the carrier density (that is, the ratio of Mn^{3+}/Mn^{4+}). The distortion of the structure leads to variations in the Mn–O bond length and the Mn–O–Mn bond angle. Meanwhile, the bandwidth (W) will also change as follows:[45]

$$W = \frac{\cos\dfrac{(\pi - \langle \mathrm{Mn-O-Mn} \rangle)}{2}}{\langle \mathrm{Mn-O} \rangle^{3.5}}. \tag{3}$$

The Co^{2+} radius surpasses that of Mn^{3+}, leading to structural distortion. As a result, the bandwidth is reduced and particle hopping becomes less challenging. Substituting Co for Mn strongly affects electron transport. Co^{2+} incorporation directly affects the Mn^{3+}/Mn^{4+} ratio, resulting in an increase in the Mn^{3+}–O^{2-}–Mn^{4+} exchange network and an enhancement in DE. Furthermore, it could be associated with the coacervation observed in the samples.[46] Comparable findings were reported in studies on $La_{0.7}Sr_{0.3}Mn_{1-x}Zn_xO_3$[47] and

$La_{0.67}Ca_{0.33}Mn_{0.85}Zn_{0.15}O_3$.[48] With the increase in Co^{2+} doping, the bandwidth W declines gradually (Table 3). Its decrease brings about a decrease in the overlap of the 3d orbitals of Mn with the 2p orbitals of O on the one hand, thus weakening the DE coupling. The weakening of the DE leads to the reduction in T_C. Due to the constraints of Hund's law, the spins of the e_g electrons are aligned in parallel with the t-localized spins in the Mn^{3+} and Mn^{4+} ions before and after the jump, which leads the system ground state into the FM metallic state. The effective jump integral in the strong coupling limit can be represented by the Anderson–Hasegawa relation as

$$t_{ij} = t^0{}_{ij} \cos(\theta_{ij}/2). \tag{4}$$

The magnitude of the jumps of electrons between near neighboring ions depends on the angle θ_{ij} between the near neighboring spins. The reduced bandwidth means that the Mn^{3+} and Mn^{4+} ions are no longer in a parallel aligned state, and the angle between the near-neighboring spins is no longer 0. The magnitude of the e_g electron hopping is reduced, and the T_C is lowered. At high temperatures, many PM substances follow a simple Curie's law. The rate of magnetization is inversely proportional to temperature. The formula is as follows:[49]

$$\chi = \frac{C}{T}, \tag{5}$$

where C is the Curie constant. However, the Curie–Weiss law is in better agreement with the experimental data. Its formula is

$$\chi = \frac{C}{T - \theta_W}, \tag{6}$$

where θ_W is the Weiss temperature. The curves in Fig. 10 are plotted from an inverse fit of the magnetization and T. The line segments fitted to the PM region are shown in red. This can be seen in Fig. 10, which shows that χ^{-1} accelerates rapidly in the case of $T > T_C$. Figure 10 indicates that the slope does not change much with the reduction in temperature and the curve tends to stabilize and flatten out when $T < T_C$. Curie–Weiss behavior manifests itself in the form of FM materials showing large magnetization at low temperatures. As the temperature increases, the magnetization decreases sharply. Higher than T_C, it becomes PM and is no longer FM. The behavior corroborates with the M–T diagram that an FM to PM transition does happen at T_C. The computed Curie temperatures θ_W are 326 K, 313 K and 290 K ($x = 0.05$, 0.075 and 0.10). A contrast indicates that the θ_W is larger than T_C. The disparity between θ_W and T_C is typically reliant on the nature of the substance itself as well as the existence of short-range ordering entities slightly above T_C.

Figure 10 illustrates the probable presence of short-range ordering bodies within the material. It is probably due to the magnetic inhomogeneity in the matter. To understand the mechanism of MCE of Co^{2+} replacing Mn^{3+} in the LSPMCO system, isothermal magnetization curves of the samples are tested in the range of 0–5 T.

The isothermal magnetization curves (M–H) are displayed in Fig. 11. The M–H curves are comparable for all samples and the intensity of saturation magnetization increased with a reduction in temperature. It can be observed that the M–H curve at low temperatures ($T < T_C$) is consistent with the FM behavior of our sample. In the case of $T > T_C$, M is comparatively small, showing typical PM behavior. Under the same condition as H, M decreases as T increases.

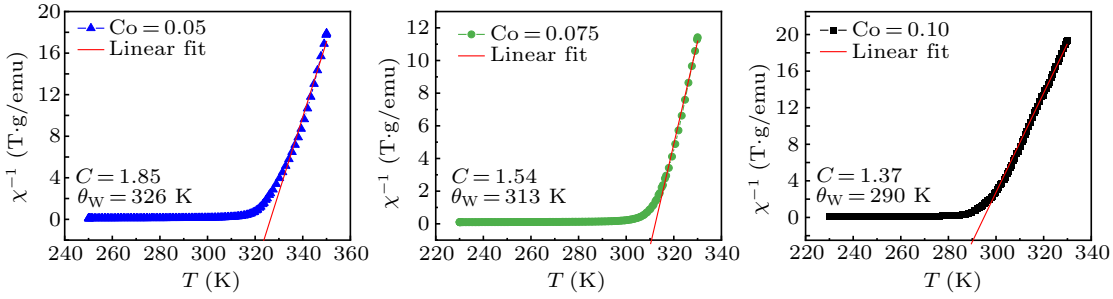


Fig. 10. Inverse susceptibility (χ^{-1}) versus T curves generated for LSPMCO ($H = 100$ Oe).

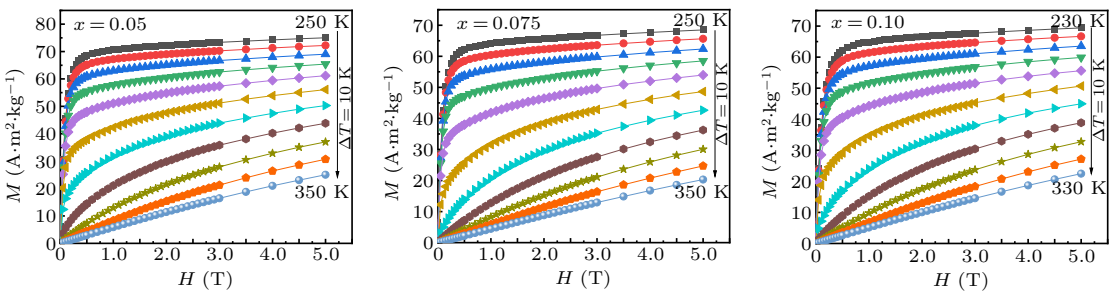


Fig. 11. Isothermal magnetization as a function of applied magnetic field at different temperatures.

3.6. Magnetic phase transition analysis

To gain deeper insight into the properties of the transition of magnetic phase transition, Fig. 12 displays an Arrott diagram for the $La_{0.67}Sr_{0.18}Pr_{0.05}Mn_{1-x}Co_xO_3$ compound. In accordance with Banerjee's criterion, the Arrott diagram with a negative sign in the slope corresponds to a first-order magnetic phase transition, and an Arrott diagram with a positive sign corresponds to a SMOPT. All slopes in the Arrott diagram are positive, indicating that all samples have undergone an FM to PM SMOPT. Furthermore, it is possible to verify the form of phase transition once more by means of the normalization curve. The normalization equation is[50]

$$\theta = \begin{cases} (T_C - T)/(T_1 - T_C), & (T \le T_C), \\ (T - T_C)/(T_2 - T_C), & (T > T_C), \end{cases} \tag{7}$$

where T_1 and T_2 are the temperatures below and above the T_C, respectively, at which the ΔS_M curve intersects. The $(\Delta S_M/-\Delta S_M^{max})$–$\theta$ curves at various H are unable to be collapsed into a single curve, and what occurs is the primary phase transition. If the curve can be collapsed into a single curve, a SMOPT occurs. All three samples in Fig. 13 can be collapsed into a single curve, verifying that it is a SMOPT.

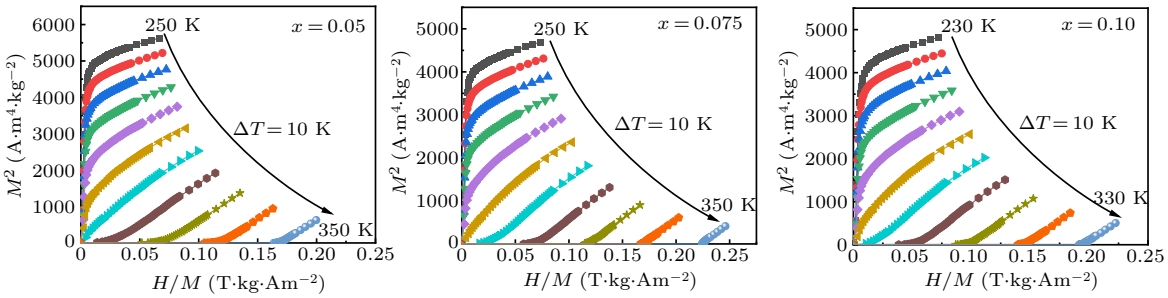


Fig. 12. The H/M versus M^2 curves (Arrott plots) for LSPMCO.

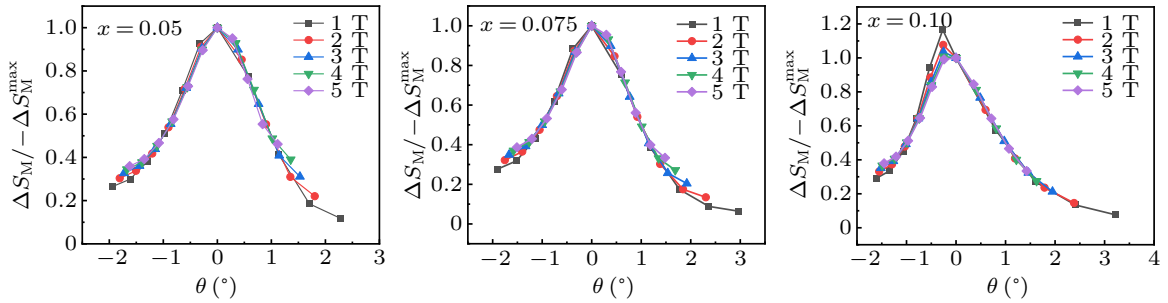


Fig. 13. Normalized curves for LSPMCO.

3.7. Critical magnetization analysis

We usually refer to the special physical properties and phenomena in and around a critical state as critical phenomena. The study of critical behavior helps us to understand and recognize the behavioral tendency of the system close to the critical point as well as the change rule of each physical quantity near the critical point, which is an important part of the phase transition theory. By calculating the critical parameters of each macroscopic physical quantity of the system in the vicinity of the phase transition point it is possible to obtain a model of the critical behavior to which the system belongs. For ferromagnetic systems, the statistical models are the mean-field model, Heisenberg model, tricritical model and Ising model. It is necessary to calculate the values of the magnetization intensity, magnetization rate and critical parameters β, γ and δ corresponding to the isothermal magnetization intensity out of the critical point.[52] Depending on the model, the critical parameters β and γ can take different values.[51] The critical temperature T_C, β and γ are defined using Arrott–Noakes diagrams with the following equations:[11,53]

$$(H/M)^{1/\gamma} = a(T - T_C)/T + bM^{1/\beta}, \tag{8}$$

$$(H/M)^{1/\gamma} = a(T - T_C)/T. \tag{9}$$

Here, a and b are constants, M is the magnetization strength, H is the magnetic field and T is the temperature. There are different models of schematic representation in Fig. 14. From Fig. 14, it can be seen that all models have almost parallel straight lines in the high magnetic field region. Therefore, it is necessary to consider the relative slope (RS). Based on the modified Arrott diagrams, we can get the RS, and it is defined as RS $= S(T)/S(T_C)$, about this determinant, while $S(T)$ and $S(T_C)$ are the slopes around T_C and at T_C, respectively.[54] Figure 15 shows the map of the RS–T of all models. It is satisfactory that the mean-field model has a value closest to 1.

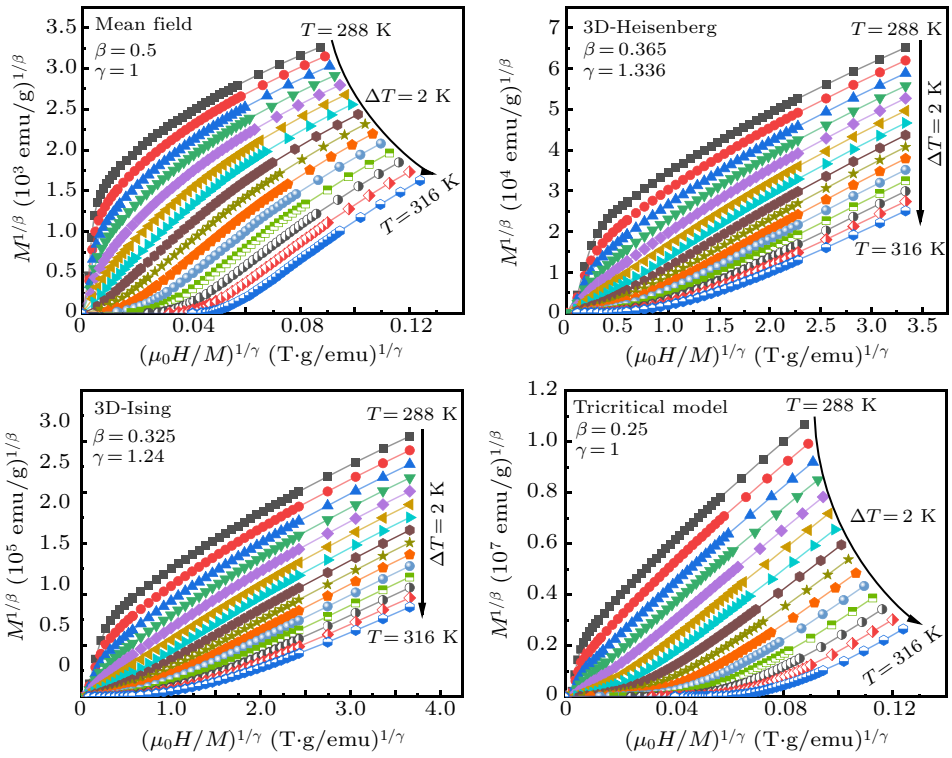


Fig. 14. (a) The mean-field model, (b) 3D-Heisenberg model, (c) 3D-Ising model and (d) tricritical model.

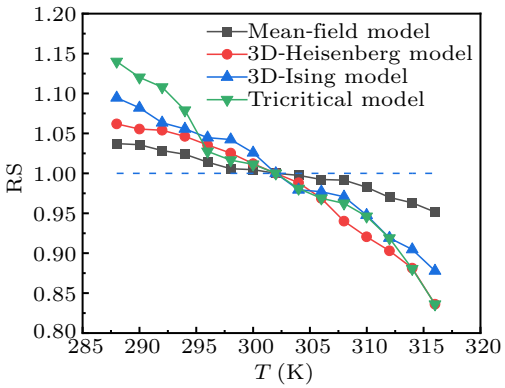


Fig. 15. The RS–T map of all models.

To get exact critical parameters, we need to fit the Arrott curve using a polynomial and derive $M^2 = 0$ and $H/M = 0$ to obtain the spontaneous magnetization strength and initial magnetization rate, respectively. According to the following equations:

$$M_{\rm S}(T) \propto |T - T_{\rm C}|^{\beta}, \quad T < T_{\rm C}, \tag{10}$$

$$\chi_0(T) \propto |T - T_{\rm C}|^{-\gamma}, \quad T > T_{\rm C}, \tag{11}$$

the experimental data can be fitted by two dotted lines to attain the critical parameters β and γ. These are shown in Fig. 16(a).

Alternatively, β and γ can be obtained by fitting using the Kouvel–Fisher method[55]

$$\frac{M_{\rm S}(T)}{{\rm d}M_{\rm S}(T)/{\rm d}T} = \frac{T - T_{\rm C}}{\beta}, \tag{12}$$

$$\frac{\chi_0^{-1}}{{\rm d}\chi_0^{-1}/{\rm d}T} = \frac{T - T_{\rm C}}{\gamma}. \tag{13}$$

The map of $\frac{M_{\rm S}(T)}{{\rm d}M_{\rm S}(T)/{\rm d}T}$ and $\frac{\chi_0^{-1}}{{\rm d}\chi_0^{-1}/{\rm d}T}$ versus temperature by linear fitting is shown in Fig. 16(b). The slopes of the straight lines are the values of β and γ. It is clear that the numerical values of the critical index and $T_{\rm C}$ calculated using the map method are similar to the numerical values of the critical parameters calculated using the KF method. Thus, the current

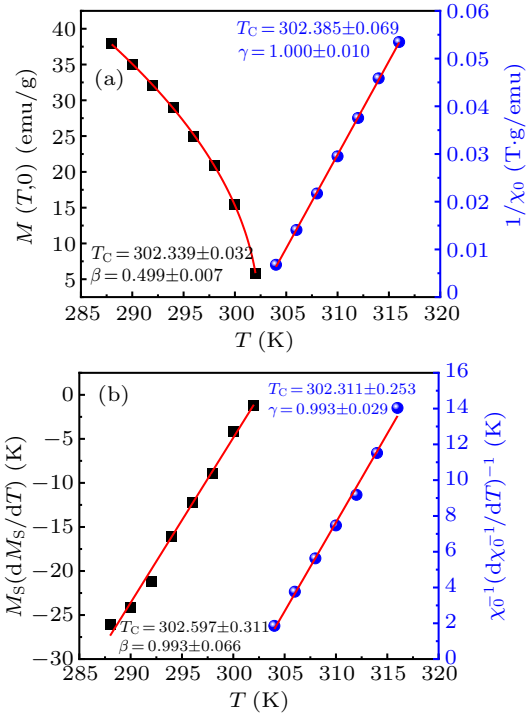


Fig. 16. (a) The spontaneous magnetization $M_{\rm S}(T)$ (left axis) and inverse susceptibility χ_0^{-1} (right axis) versus temperature for LSPMCO. (b) The Kouvel–Fisher plots for LSPMCO.

research methodology for calculating the criticality properties is effective and feasible.

The effectiveness of the critical indices can be determined by examining the relationship between the critical parameters β, γ and δ. Based on $M = DH^{1/\delta}$, $\varepsilon = 0$ and $T = T_C$, we drew $\ln(M)$ versus $\ln(H)$ to determine the critical parameters δ in Fig. 17. δ can be compared to the value obtained theoretically from Widom's scalar law formula

$$\delta = 1 + \frac{\lambda}{\beta}. \tag{14}$$

The resultant theoretical and experimental values are both similar, ensuring the reliability of the obtained β and γ values.[56] All the above research data identifies the sample as a second-order phase change material, which has less thermal hysteresis relative to the first-order phase change hysteresis and has greater potential for application.

3.8. Magnetothermal analysis

The variation of magnetic entropy is achieved through the insulated variation of T with a magnetic field. According to Maxwell's thermodynamic relation[57]

$$\left(\frac{\partial S}{\partial H}\right)_T = \left(\frac{\partial M}{\partial T}\right)_H, \tag{15}$$

the ΔS_M can be obtained by the following equation:

$$\Delta S_M(\mu_0 H) = \int_0^{\mu_0 H_{max}} \left(\frac{\partial M(T, \mu_0 H)}{\partial T}\right)_{\mu_0 H} \mathrm{d}(\mu_0 H). \tag{16}$$

Since the magnetization was measured at both discrete magnetic fields and T intervals, Eq. (16) can be approximated to obtain the following equation:

$$\Delta S(\mu_0 H) = \sum_i \frac{M_{i+1}(T_{i+1}, H) - M_i(T_i, H)}{T_{i+1} - T_i} \Delta H, \tag{17}$$

in which M_i and M_{i+1} are the experiment magnetization values at temperatures T_i and T_{i+1}, respectively.

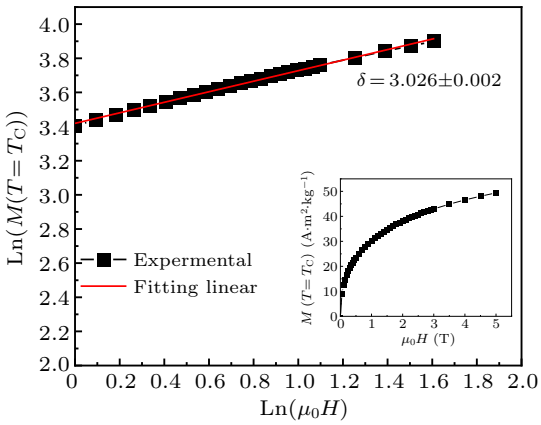


Fig. 17. The critical parameter δ is determined by $\ln(M)$ versus $\ln(H)$.

The ΔS_M of LSPMCO at different H and T are given in Fig. 18. The graph indicates that at a constant temperature, the ΔS_M gradually increases as the magnetic field increases. This can be due to the fact that the stronger magnetic field is more likely to realign the local spin arrangements, resulting in an increase in the ΔS_M. In addition, the ΔS_M shows a tendency to decline with increasing Co^{2+} doping. This may be due to the change in the percentage of Mn^{4+}/Mn^{3+} due to the addition of Co^{2+}. The SE effect is introduced to suppress the DE, leading to a decrease in the ΔS_M. On the other hand, the Co magnetic moment is different from that of Mn. The properties of the magnetism of a substance are usually indicated by the magnetic moment μ, which is a function of an argument that is immediately associated with the number of unpaired electrons. The relationship between μ and χ is[58]

$$\chi = \frac{N_A \beta^2 \mu^2}{3kT}, \tag{18}$$

where N_A is Avogadro's constant ($N_A = 6.0232 \times 10^{-23}$), β is the Bohr magneton and k is Boltzmann's constant ($k = 1.38016 \times 10^{-23}$ J/K). The experimental effective magnetic moment (μ_{eff}^{exp}) can be calculated by combining the following equation:

$$\mu = 2.83\sqrt{C}. \tag{19}$$

The value of the theoretical magnetic moment is obtained from the following relation:[59]

$$\mu_{eff}^{the} = \sqrt{0.95[(0.67-x)u_{eff}^2(Mn^{3+}) + (0.28+x)u_{eff}^2(Mn^{4+}) + 0.05u_{eff}^2(Pr^{3+}) + xu_{eff}^2(Co^{3+})}. \tag{20}$$

The values of μ_{eff}^{exp} and μ_{eff}^{the} are calculated in Table 3. Based on the table, it can be assumed that the Co^{2+} doping μ_{eff}^{exp} diminishes, and ΔS_M also decreases at the beginning of the phase transition. In addition, the reason that there is a difference between the value of μ_{eff}^{the} and μ_{eff}^{exp} is usually due to the presence of short-range FM interactions beyond the T_C.

Table 3. The T_C, θ_W (CW temperature), C (Curie constant), μ_{eff}^{the}, and μ_{eff}^{exp} of LSPMCO.

x	0.05	0.075	0.10
T_C (K)	315.7	302.2	289.2
θ_W (K)	326	313	290
C (μ_B·K/T)	1.85	1.54	1.37
μ_{eff}^{exp} (μ_B)	3.85	3.51	3.31
μ_{eff}^{the} (μ_B)	4.42	4.41	4.39

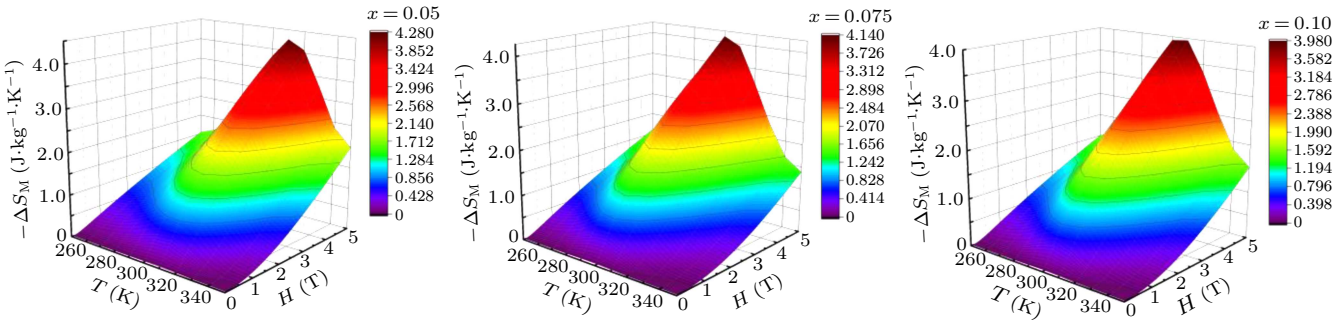


Fig. 18. Temperature dependence of the magnetic entropy change ($-\Delta S_{\rm M}$) at different applied magnetic fields.

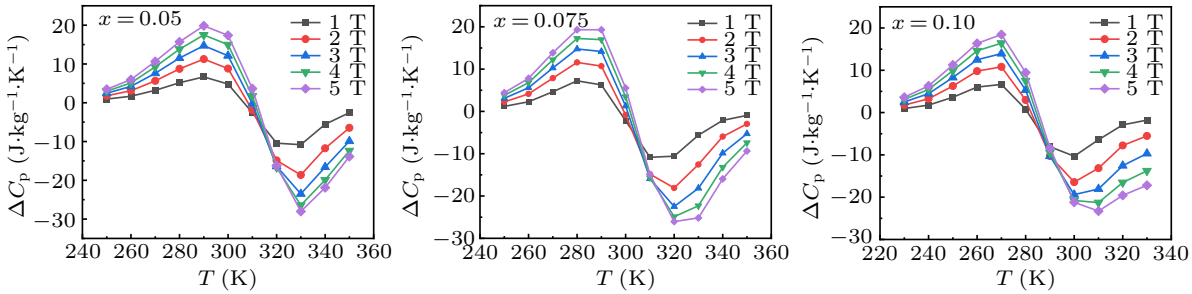


Fig. 19. Variation in the specific heat capacity with T for LSPMCO (1–5 T).

The total of the values of the combined positive and negative fractions of the heat capacity is the field's response to the entire specific heat. Heat capacity influences the refrigeration or heating ability of magnetic materials and represents a useful indicator of the magnetocaloric effect. On the basis of thermodynamic theory, the variation of magnetic entropy is given by the equation of specific heat capacity[60]

$$\Delta S_{\rm M} = \int_0^T \frac{C_{\rm p}(T,\mu_0 H) - C_{\rm p}(T,0)}{T}\,{\rm d}T. \tag{21}$$

The variation of H results in a variation of the specific heat. The heat capacity is obtained by the following formula:

$$\Delta C_{\rm p} = C_{\rm p}(T,\mu_0 H) - C_{\rm p}(T,0) = T\frac{\partial \Delta S_{\rm M}^{\rm max}(T,\mu_0 H)}{\partial T}. \tag{22}$$

Figure 19 shows that the thermal fusion exhibits an increasing and then decreasing trend. The magnitude of $\Delta C_{\rm p}^{\rm max}$ as well as $\Delta C_{\rm p}^{\rm min}$ is monotonic as H increases. The potential of the material as a room-temperature magnetic refrigeration material is further demonstrated by the heat capacity of the samples. The RCP is a significant parameter for judging its performance, and the formula for calculating the RCP is[61]

$$\mathrm{RCP} = -\Delta S_{\rm Max} \times \delta T_{\rm FWHM}, \tag{23}$$

where $\delta T_{\rm FWHM}$ is the magnitude of the half-peak width of the maximum in the magnetic entropy variation curve. The relevance between both RCP and H is demonstrated in Fig. 20. It is clear from the diagram that the RCP of $La_{0.67}Sr_{0.28}Pr_{0.05}Mn_{1-x}Co_xO_3$ ($x = 0.05$, 0.075, 0.10) gradually diminishes with the increase in doping. This occurs provided that there are two aspects. One is that the $\Delta S_{\rm M}$ decreases with the increase in doping. The other is that Mn^{4+} increases and Mn^{3+} decreases after Co^{2+} replaces Mn^{3+}. There is no significant additional half-peak width under the complex effect of DE and SE. The $\Delta S_{\rm M}$ decreases with no significant increase in the half-peak width, and therefore the RCP diminishes.

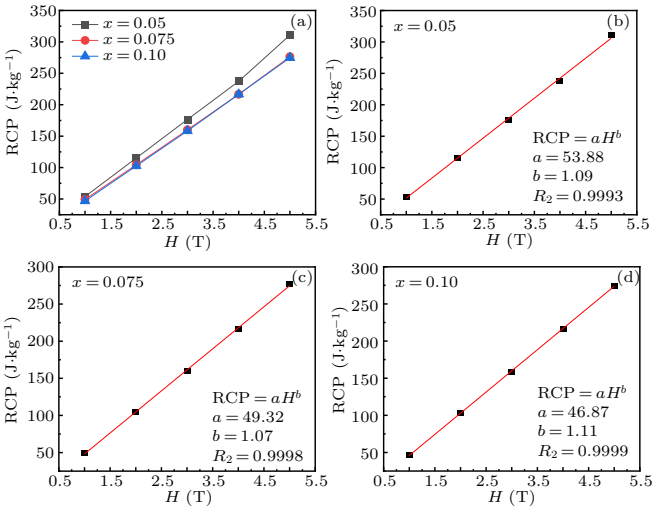


Fig. 20. Relative cooling power plot for LSCMCO ($x = 0.05$, 0.075 and 0.10) and their fitting curves.

When $H = 5$ T, the values of LSPMCO with other materials $T_{\rm C}$, $-\Delta S_{\rm M}^{\rm max}$, RCP and H are as listed in Table 4. The comparison reveals that LSPMCO has superior relative cooling efficiency and $\Delta S_{\rm M}$ at $x = 0.05$. It has the potential for further research and to be developed as a magnetic refrigeration material.

Table 4. The comparison of LSPMCO with previously investigated magnetically cooled materials in terms of T_C, H, $-\Delta S_M^{max}$ and RCP.

Materials	H (T)	T_C (K)	$-\Delta S_M^{max}$ (J/kg·K)	RCP (J/K)	Ref.
Gd	2	294	5	196	[62]
$La_{0.67}Sr_{0.33}MnO_3$	2	354	1.15	88	[63]
$La_{0.67}Ba_{0.33}MnO_3$	5	292	1.48	161	[64]
$La_{0.75}Ho_{0.05}Sr_{0.2}MnO_3$	2	310	1.48	73.69	[65]
$La_{0.75}Sr_{0.15}Ca_{0.15}MnO_3$	5	310	5.8	195.21	[66]
$La_{0.57}Nd_{0.1}Sr_{0.13}Ag_{0.2}MnO_3$	5	307	5.08	146.74	[67]
$La_{0.67}Sr_{0.33}Mn_{0.85}V_{0.15}O_3$	5	292	5.24	258	[68]
$La_{0.6}Pr_{0.2}Sr_{0.2}MnO_3$	5	244	4.16	174.7	[69]
$La_{0.8}Ca_{0.2}Mn_{0.9}Co_{0.1}O_3$	5	–	2.63	144.54	[70]
$La_{0.8}Ca_{0.2}Mn_{0.9}Co_{0.1}O_3$	5	–	2.34	224.07	[70]
$La_{0.7}Sr_{0.3}Mn_{0.95}Co_{0.05}O_3$	1	300	1.17	46.8	[71]
$La_{0.7}Sr_{0.3}Mn_{0.90}Co_{0.10}O_3$	1	260	0.92	54.3	[71]
$La_{0.8}Na_{0.2}Mn_{0.94}Co_{0.06}O_3$	5	255	3.95	260	[72]
$La_{0.55}Pr_{0.1}Sr_{0.35}Mn_{0.95}Ti_{0.05}O_3$	3	288	2.78	118.85	[73]
$La_{0.67}Ca_{0.13}Ba_{0.2}Mn_{0.96}Co_{0.04}O_3$	1.6	272	2.68	–	[74]
$La_{0.67}Ba_{0.22}Sr_{0.11}Mn_{0.8}Co_{0.2}O_3$	5	228	2.12	270	[75]
$La_{0.67}Sr_{0.28}Pr_{0.05}Mn_{0.95}Co_{0.05}O_3$	5	316	4.26	311.54	this study
$La_{0.67}Sr_{0.28}Pr_{0.05}Mn_{0.95}Co_{0.05}O_3$	5	302	4.13	276.43	this study
$La_{0.67}Sr_{0.28}Pr_{0.05}Mn_{0.95}Co_{0.05}O_3$	5	289	3.96	274.79	this study

4. Conclusion

Samples have been synthesized using the sol–gel technique. The structure and morphology of the samples as well as the magnetocaloric effect are also tested and analyzed. The XRD diffraction results indicate a pure phase excluding any impurities. The material has a rhombohedral structure belonging to the R-3c space group. SEM yields samples that are irregular particles of submicron size. The samples undergo an SMOPT in the vicinity of T_C from FM to PM. XPS confirms that the proportion of Mn^{4+}/Mn^{3+} changes with the amount of doping. Critical behavior analysis confirms that the LSPMCO critical behavior is in agreement with the mean-field model. The magnetic hysteresis and thermal hysteresis of the SMOPT are much smaller, providing better efficiency. At a doping level of 0.075 and a temperature of 302 K, T_C is closest to ambient temperature. The optimal performance at 5 T is achieved with a doping level of 0.05, resulting in a maximum $-\Delta S_M^{max}$ of 4.26 J/kg·K and RCP maximum of 311.54 J/kg.

Acknowledgement

Project supported by the National Natural Science Foundation of China (Grant No. 52162038).

References

[1] Lyubina J 2017 *J. Phys. D: Appl. Phys.* **50** 053002
[2] Balli M, Jandl S, Fournier P and Kedous-Lebouc A 2017 *Appl. Phys. Rev.* **4** 021305
[3] Chaudhary V and Ramanujan R 2016 *Scientific Reports* **6** 35156
[4] Chaudhary V, Chen X and Ramanujan R V 2019 *Progress in Materials Science* **100** 64
[5] Brück E 2005 *J. Phys. D: Appl. Phys.* **38** R381
[6] Bai J, Dong Q, Zhang L, Liu Q, Cheng J, Liu P, Li C, Sun Y, Huang Y and Ren Z 2023 *Chin. Phys. Lett.* **40** 127501
[7] Zhang Y, Shi Y G, Wang L C, Zheng X Q, Liu J, Jin Y X, Zhang K W, Liu H X, Zong S T and Sun Z G 2022 *Chin. Phys. B* **31** 077501
[8] Yu S L, Tian L, Wang J F, Zhao X G, Li D, Mo Z J and Li B 2024 *Chin. Phys. B* **33** 057502
[9] Shull R D 1993 *IEEE Transactions on Magnetics* **29** 2614
[10] Chaudhary V, Maheswar Repaka D, Chaturvedi A, Sridhar I and Ramanujan R 2014 *J. Appl. Phys.* **116** 163918
[11] Franco V, Blázquez J, Ingale B and Conde A 2012 *Annual Review of Materials Research* **42** 305
[12] Chen W, Hong B, Zeng Y, Wang X, Peng X, Li J and Xu J 2023 *J. Alloys Compd.* **933** 167625
[13] Smith A, Bahl C R, Bjørk R, Engelbrecht K, Nielsen K K and Pryds N 2012 *Advanced Energy Materials* **2** 1288
[14] Markovich V, Wisniewski A and Szymczak H 2014 *Handbook of magnetic materials* (Elsevier) pp. 1–201
[15] Dhahri J, Mnefgui S, Hassine A B, Tahri T, Oumezzine M and Hlil E 2018 *Physica B* **537** 93
[16] Akça G, Çetin S K and Ekicibil A 2017 *Ceramics International* **43** 15811
[17] Liu Z, Lin W, Zhou K and Yan J 2018 *Ceramics International* **44** 2797
[18] Millis A 1998 *Nature* **392** 147
[19] Fontcuberta J, Martinez B, Seffar A, Pinol S, Garcia-Munoz J and Obradors X 1996 *Phys. Rev. Lett.* **76** 1122
[20] Goldschmidt V M 1926 *Naturwissenschaften* **14** 477
[21] Kursun C, Gogebakan M, Uludag E, Bozgeyik M S and Uludag F S 2018 *Scientific Reports* **8** 13083
[22] Das S and Dey T 2007 *J. Phys. D: Appl. Phys.* **40** 1855
[23] Moradi J, Ghazi M, Ehsani M and Kameli P 2014 *Journal of Solid State Chemistry* **215** 1
[24] Bellakki M B, Shivakumara C, Vasanthacharya N and Prakash A 2010 *Materials Research Bulletin* **45** 1685
[25] Kumar S, Dwivedi G, Kumar S, Mathur R, Saxena U, Ghosh A, Joshi A G, Yang H and Chatterjee S 2015 *Dalton Transactions* **44** 3109
[26] Liu Y, Sun T, Dong G, Zhang S, Chu K, Pu X, Li H and Liu X 2019 *Ceramics International* **45** 17467
[27] Reddy M P, Shakoor R and Mohamed A 2016 *Materials Chemistry and Physics* **177** 346
[28] Sheela G E, Manimaran D, Joe I H, Rahim S and Jothy V B 2015 *Spectrochimica Acta Part A: Molecular and Biomolecular Spectroscopy* **143** 40
[29] Koushalya P and Manjunatha A 2021 *Applied Surface Science Advances* **6** 100135
[30] Rajan A, Sharma M and Sahu N K 2020 *Scientific Reports* **10** 15045
[31] Kucharczyk B and Tylus W 2007 *Catalysis Letters* **115** 122

[32] Wang X, Zhang C, Zang G, Lv S and Li L 2015 *J. Alloys Compd.* **637** 277
[33] Zhang P, Guan G, Khaerudini D S, Hao X, Xue C, Han M, Kasai Y and Abudula A 2014 *Journal of Power Sources* **266** 241
[34] Gu Q, Wang L, Wang Y and Li X 2019 *Journal of Physics and Chemistry of Solids* **133** 52
[35] Biesinger M C, Payne B P, Grosvenor A P, Lau L W, Gerson A R and Smart R S C 2011 *Applied Surface Science* **257** 2717
[36] Lee S, Yoon S, Chung I, Hartwig A and Kim B 2011 *Handbook of X-ray Photoelectron Spectroscopy* (Waltham: Perkin-Elmer Corporation)
[37] Tabata K, Hirano Y and Suzuki E 1998 *Applied Catalysis A: General* **170** 245
[38] Chen J, Shen M, Wang X, Qi G, Wang J and Li W 2013 *Applied Catalysis B: Environmental* **134** 251
[39] Chen S, Hao Y, Chen R, Su Z and Chen T 2021 *J. Alloys Compd.* **861** 158584
[40] Uthaman B, Anand K, Rajan R K, Kyaw H H, Thomas S, Al-Harthi S, Suresh K and Varma M R 2015 *RSC Advances* **5** 86144
[41] Dinamarca R, Garcia X, Jimenez R, Fierro J and Pecchi G 2016 *Materials Research Bulletin* **81** 134
[42] Xia W, Liu X, Jin F, Jia X, Shen Y and Li J 2020 *Electrochimica Acta* **364** 137274
[43] Pendashteh A, Palma J, Anderson M and Marcilla R 2016 *RSC Advances* **6** 28970
[44] Choudhury T, Saied S, Sullivan J and Abbot A 1989 *J. Phys. D: Appl. Phys.* **22** 1185
[45] Medarde M, Mesot J, Lacorre P, Rosenkranz S, Fischer P and Gobrecht K 1995 *Phys. Rev. B* **52** 9248
[46] Al-Yahmadi I, Gismelseed A, Al Ma'Mari F, Al-Rawas A, Al-Harthi S, Yousif A, Widatallah H, Elzain M and Myint M 2021 *J. Alloys Compd.* **875** 159977
[47] Sotirova-Haralambeva E, Wang X, Liu K, Silver T, Konstantinov K and Horvat J 2003 *Science and Technology of Advanced Materials* **4** 149
[48] Xu M X and Jiao Z K 1999 *Journal of Materials Science Letters* **18** 1307
[49] Hcini S, Boudard M and Zemni S 2014 *Appl. Phys. A* **115** 985
[50] Franco V, Blázquez J and Conde A 2008 *J. Appl. Phys.* **103** 07B316
[51] Stanley H E 1999 *Rev. Mod. Phys.* **71** S358
[52] Stanley H E and Ahlers G 1973 *Introduction to phase transitions and critical phenomena* (American Institute of Physics)
[53] Franco V, Blázquez J, Ipus J, Law J, Moreno-Ramírez L and Conde A 2018 *Progress in Materials Science* **93** 112
[54] Schwartz A, Scheffler M and Anlage S M 2000 *Phys. Rev. B* **61** R870
[55] Kouvel J S and Fisher M E 1964 *Phys. Rev.* **136** A1626
[56] Widom B 1965 *The Journal of Chemical Physics* **43** 3898
[57] Pecharsky V K and Gschneidner Jr K A 1999 *J. Magn. Magn. Mater.* **200** 44
[58] Kochmański M, Paszkiewicz T and Wolski S 2013 *Euro. J. Phys.* **34** 1555
[59] Buschow K H J and Boer F R 2003 *Physics of magnetism and magnetic materials* Vol. 7 (Springer)
[60] Raoufi T, Ehsani M and Khoshnoud D S 2016 *J. Alloys Compd.* **689** 865
[61] Guo Z, Du Y, Zhu J, Huang H, Ding W and Feng D 1997 *Phys. Rev. Lett.* **78** 1142
[62] Lu C, Dong S, Wang K, Gao F, Li P, Lv L and Liu J M 2007 *Appl. Phys. Lett.* **91** 172107
[63] Wang G, Li L, Zhao Z, Yu X and Zhang X 2014 *Ceramics International* **40** 16449
[64] Morelli D T, Mance A M, Mantese J V and Micheli A L 1996 *Journal of applied physics* **79** 373
[65] Ehsani M, Kameli P, Razavi F, Ghazi M and Aslibeiki B 2013 *J. Alloys Compd.* **579** 406
[66] Dhahri A, Jemmali M, Dhahri E and Valente M 2015 *J. Alloys Compd.* **638** 221
[67] Gharbi S, Marouani Y, Issaoui F, Dhahri E, Hlil E, Barille R and Costa B 2020 *Journal of Materials Science: Materials in Electronics* **31** 11983
[68] Mnefgui S, Zaidi N, Dhahri A, Hlil E and Dhahri J 2014 *Journal of Solid State Chemistry* **215** 193
[69] Zarifi M, Kameli P, Mansouri M, Ahmadvand H and Salamati H 2017 *Solid State Commun.* **262** 20
[70] Turki D, Remenyi G, Mahmood S, Hlil E, Ellouze M and Halouani F 2016 *Materials Research Bulletin* **84** 245
[71] Zhang P, Yang H, Zhang S, Ge H and Hua S 2013 *Physica B* **410** 1
[72] Laouyenne M, Baazaoui M, Hlil E, Oumezzine M and Farah K 2022 *Journal of Superconductivity and Novel Magnetism* **35** 2889
[73] Guedri A, Mnefgui S, Hcini S, Hlil E and Dhahri A 2021 *Journal of Solid State Chemistry* **297** 122046
[74] Xiao G, He W, Yang T, Huang G, Wang T and Huang J 2019 *Current Applied Physics* **19** 424
[75] Ben Jemaa F, Mahmood S, Ellouze M, Hlil E and Halouani F 2015 *Journal of Materials Science* **50** 620